Shi, Junjie; Pršlja, Paulina; Suominen, Milla; Jin, Benjin; Lahtinen, Jouko; Moumaneix, Lilian; Kong, Xiangze; Kallio, Tanja

Mn-doped Bi_2O_3 grown on PTFE-treated carbon paper for electrochemical CO_2-to-formate production

Published in:
Journal of Catalysis

DOI:
10.1016/j.jcat.2024.115798

Published: 01/12/2024

Document Version
Publisher's PDF, also known as Version of record

Please cite the original version:
Shi, J., Pršlja, P., Suominen, M., Jin, B., Lahtinen, J., Moumaneix, L., Kong, X., & Kallio, T. (2024). Mn-doped Bi_2O_3 grown on PTFE-treated carbon paper for electrochemical CO_2-to-formate production. *Journal of Catalysis*, *440*, Article 115798. https://doi.org/10.1016/j.jcat.2024.115798

Journal of Catalysis 440 (2024) 115798

Contents lists available at ScienceDirect

Journal of Catalysis

journal homepage: www.elsevier.com/locate/jcat

Research article

Mn-doped Bi_2O_3 grown on PTFE-treated carbon paper for electrochemical CO_2-to-formate production

Junjie Shi [a], Paulina Pršlja [a], Milla Suominen [a,*], Benjin Jin [a], Jouko Lahtinen [b], Lilian Moumaneix [a], Xiangze Kong [a], Tanja Kallio [a,*]

[a] Department of Chemistry and Materials Science, School of Chemical Engineering, Aalto University, P.O. Box 16100 00076, Aalto, Finland
[b] Department of Applied Physics, School of Science, Aalto University, P.O. Box 15100 00076, Aalto, Finland

ARTICLE INFO

Keywords:
CO_2 electrochemical reduction
Mn-doped Bi_2O_3
In situ Raman
Phase transition
Wet-proofed substrate

ABSTRACT

BiO_x shows promising selectivity in catalyzing the electrochemical reduction of CO_2 to formate, but the process suffers from high overpotential and a low rate. Moreover, the active sites are still ambiguous under electrochemical conditions. Herein, we introduce Mn-doping to enhance the activity of binder-free Bi_2O_3 and elaborate on active sites through ***in situ*** Raman and density functional theory (DFT) analyses. The Mn-doped Bi_2O_3 transforms to Mn-doped $Bi_2(CO_3)O_2$ in $KHCO_3$ and subsequently reduces to Mn-modified metallic Bi under cathodic potentials. The undoped Bi_2O_3 is found to follow the same phase transitions but at a different rate. The DFT analyzes the impact of doping the Bi(012) with Mn and indicates significantly improved selectivity for formate generation. Further, the importance of the substrate's hydrophobicity for long-term stability is demonstrated. This study offers in-depth insights into the design and understanding of doped BiO_x-based electrodes for CO_2 reduction.

1. Introduction

Transforming CO_2 into useful chemicals by electrochemical reduction (CO_2RR) offers a potential way to close the carbon loop when powered by renewable energies [1]. The thermodynamically stable CO_2 molecule, the complex pathways, and the competing hydrogen evolution reaction (HER) in an aqueous solution are the main obstacles to achieving desired activity [2]. Therefore, rational design of electrocatalysts and electrode structure are key factors for achieving selective and efficient CO_2RR. Formate is one of the value-added chemicals produced by CO_2RR, which can be widely used in a variety of chemical engineering industries [3]. In addition, electrochemical CO_2-to-formate production is the most technologically and economically profitable approach to realize efficient utilization of both feedstock and energy [3].

Due to their high abundance, low toxicity, and promising formate selectivity, Bi-based electrocatalysts have drawn attention for CO_2RR [4,5]. However, bulk Bi electrocatalysts typically still suffer from low current density and a high reaction overpotential, especially in a near-neutral electrolyte [6,7]. In this scenario, various attempts have been made to modulate the CO_2RR performance on Bi-based electrocatalysts through defect creation [8,9] and morphological engineering [10,11], as well as supporting [12–14]. Heteroatom doping is another facile and efficient way to alter the catalytic performance [7,15]. Particularly, the incorporation of transition metals such as V [16], Fe [17], Ni [18], Cu [19], Zn [20], Pd [21], and Cd [20] have been reported to tune the intrinsic properties of Bi-based electrocatalysts by altering their coordination environment and further improving the adsorption of species. MnO_x has shown great potential in the electrochemical CO_2-to-CO conversion [22,23], and when Mn is used as a dopant in SnO_2 [24], it also enhances CO_2-to-formate conversion. Therefore, synthesizing Mn-doped Bi-based electrocatalysts in appropriate combinations is desirable for effective CO_2RR.

Under applied potentials, interstingly, the phase change of Bi-based electrocatalysts (e.g. BiO_x, $Bi_2(CO_3)O_2$, and BiOX, where X = Cl, Br, I) makes the real active sites ambiguous [25–27]. It is still debatable whether Bi-based electrocatalysts could reduce into metallic Bi or maintain a high valence state during the process [27,28]. Revealing the real active sites of Bi-based electrocatalysts during CO_2RR is of great importance for elucidation of the reaction mechanism and *in situ* Raman spectroscopy can be applied as a powerful technique to study the electrode surfaces under an electrochemical process with real-time measurements [29,30].

---

* Corresponding authors.
E-mail addresses: milla.suominen@aalto.fi (M. Suominen), tanja.kallio@aalto.fi (T. Kallio).

https://doi.org/10.1016/j.jcat.2024.115798
Received 16 July 2024; Received in revised form 30 September 2024; Accepted 15 October 2024

Apart from the electrocatalyst, binder, and substrate in the electrode preparation process can affect CO_2RR [31]. The catalytic performance can easily be altered by tuning substrates [24,32,33], especially carbon-based substrates [32,33]. The hydrophobicity modification on the carbon-based substrates is crucial in CO_2RR, which can improve gas transport and repel electrolyte permeation. Although there are numerous studies over catalyst powder/binder drop-casted on the substrate with different hydrophobicity [33–35], it is usually overlooked when applied to a binder-free architecture.

Herein, we grew Mn-doped Bi_2O_3 (Mn-Bi_2O_3) on wet-proofed substrates by a facile method and studied the Mn-doping effects on Bi_2O_3 activity for CO_2RR. To reveal the active catalyst during the reaction, extensive *in situ* Raman and *ex situ* physico-chemical characterizations were performed, and the results were applied to further elaborate the reaction mechanisms with computational methods. We also applied different substrates to demonstrate the importance of the electrode structure for the stability of the novel doped catalyst material. This study offers in-depth insights into the design and understanding of doped BiO_x-based electrodes for CO_2RR.

2. Methods

2.1. Materials

Bismuth(III) nitrate pentahydrate ($Bi(NO_3)_3{\cdot}5H_2O$, 98.0 %), manganese(II) nitrate hexahydrate ($Mn(NO_3)_2{\cdot}6H_2O$, ≥98.0 %), ethylene glycol (ReagentPlus®, ≥99.0 %), Nafion® dispersion (5 wt%), 2-Propanol (suitable for HPLC, 99.9 %), and potassium bicarbonate ($KHCO_3$, 99.7 %) were purchased from Sigma-Aldrich. Ethanol AA grade was purchased from Altia Oyj. All chemicals were used as supplied. Water from a Synergy purification system (18.2 MΩ cm at 25 °C) was used to prepare all aqueous solutions. Wet-proofed carbon paper (TGP-H-120, 5 wt% PTFE treated) and carbon paper (AvCarb MGL370) were purchased from FuelCellsEtc and cut into 2.5 cm × 2.5 cm pieces. Nafion 115 membrane was purchased from Ion Power and treated with 5 % H_2O_2 for 60 min, water for 30 min, 0.5 M H_2SO_4 for 60 min, and finally, 3 times in water all at 100 °C. CO_2 (99.995 %) from Woikoski was used as supplied.

2.2. Working electrode preparation

Growth of Mn-doped Bi_2O_3 on the wet-proofed carbon paper (Mn-Bi_2O_3): Mn-doped Bi_2O_3 was grown on the wet-proofed (PTFE modified) carbon paper through a modified solvothermal method [36,37], followed by calcination (see **Scheme S1**). In a typical procedure, 1 mmol of $Bi(NO_3)_3{\cdot}5H_2O$ and 53 μmol of $Mn(NO_3)_2{\cdot}6H_2O$ were dissolved in 6 mL of ethylene glycol and 12 mL of ethanol in a 50 mL autoclave (Metalworking) to form a homogeneous solution. A piece of the wet-proofed carbon paper was placed aslant in the autoclave and held for 1 h at room temperature before thermal treatment at 160 °C for 8 h. The as-obtained electrodes were rinsed with ethanol and further calcinated in the air at 300 °C for 1 h with a heating rate of 5 °C min^{-1} to convert $BiO_{2\text{-}x}$ into β-Bi_2O_3 [38]. To optimize the synthesis procedure, varying amounts of $Mn(NO_3)_2{\cdot}6H_2O$ (namely 31, 75, 107, 111, and 176 μmol) were also studied.

Growth of Bi_2O_3 supported on the wet-proofed carbon paper (Bi_2O_3): Bi_2O_3 was grown on the wet-proofed carbon paper through the same method without the addition of $Mn(NO_3)_2{\cdot}6H_2O$.

Growth of Mn-doped Bi_2O_3 on unmodified carbon paper (Mn-Bi_2O_3 on unmodified carbon paper) and hydrophilic carbon paper (Mn-Bi_2O_3 on hydrophilic carbon paper): To study the effect of substrates, Mn-doped Bi_2O_3 was also grown on unmodified carbon paper and hydrophilic carbon paper following the optimized procedure. Unmodified carbon paper was AvCarb MGL370 while the hydrophilic carbon paper was AvCarb MGL370 treated by soaking in 65 % nitric acid overnight, followed by thorough rinsing with water and ethanol and drying in air.

2.3. Characterizations

X-ray diffraction (XRD): XRD measurements were performed with the electrodes attached to the sample holder using a Panalytical X'PERT PRO MPD Alpha 1 diffractometer and Cu K_α radiation (λ = 0.15418 nm, 45 kV, 40 mA) in a 2θ range of 10° to 90°.

Transmission electron microscopy (TEM): Catalyst powder was first dispersed in ethanol by sonicating the Mn-Bi_2O_3 or Bi_2O_3 electrodes and then the dispersant was drop-casted on holey carbon films (Agar Scientific, AGS147-3). TEM and TEM-EDS analysis were acquired using a JEOL JEM-2800FS microscope at an accelerating voltage of 200 kV.

Scanning electron microscopy (SEM): SEM images were taken with the electrode's pieces attached to the sample holder with conducting tape using a JEOL JIB-4700F microscope at an accelerating voltage of 5 kV or a Tescan Mira3 microscope at an accelerating voltage of 5 kV.

X-ray photoelectron spectroscopy (XPS): A small expansion to make the test symmetrical XPS measurements from electrode pieces were performed at a 0.3 mm × 0.7 mm analysis area with the charge neutralizer using the Kratos Axis Ultra system equipped with a monochromatic Al-K_α X-ray source. The wide scans and the high-resolution scans were performed with 80 eV pass energy at 1 eV energy step and 40 eV pass energy at 0.1 eV step size, respectively. The energy calibration is made using the C 1 s at 284.8 eV.

Inductively coupled plasma-optical emission spectrometry (ICP-OES): The fresh and used electrodes were soaked in 5 % nitric acid to dissolve the active materials. The Mn and Bi content were detected by using a 5990 Agilent ICP-OES equipment by analyzing the as-prepared solution.

Contact angle measurement: Contact angle measurements of the electrodes were made using a Theta Flex optical tensiometer with 5 μL of 0.5 M $KHCO_3$.

2.4. Electrochemical studies

The electrolysis of CO_2 was performed in a customized flow-through mode cell (see the configuration in **Scheme S2**) at room temperature consisting of a working electrode prepared as described above, an Iridium Mixed Metal Oxide plate (ElectroCell) as a counter electrode, and a leak-free Ag/AgCl reference electrode (Innovative Instruments) coupled with an IviumStat.XRi potentiostat. CO_2 was bubbled onto the working electrode at 11 mL min^{-1}, and CO_2-satruated 0.5 M $KHCO_3$ (pH = 7.3) was used as the electrolyte with the flow rate of 11 mL min^{-1} in both anode and cathode compartments.

Before electrolysis, cyclic voltammetry (CV) test was performed from − 0.93 V to − 1.93 V (vs. Ag/AgCl) at a scan rate of 50 mV s^{-1} for 5 scans. After recording the CVs, short-term electrolysis (60 min or less) was performed with a controlled potential method from − 1.33 V to − 1.53 V with 50 mV interval, and − 1.53 V to − 1.83 V (vs. Ag/AgCl) with 100 mV interval, respectively. For the long-term stability test, electrolysis was performed with a controlled current method at − 25 mA cm^{-2}. During electrolysis, the gaseous products were analyzed by gas chromatography (μ-GC, Agilent 990) equipped with two columns (MoleSieve 5A for natural gases and PoraPlot for hydrocarbons) and micro-machined thermal conductivity detectors (TCD). Liquid products were collected and quantified by High-Performance Liquid Chromatography (HPLC, Waters 2690) using AMinex column HPX-87X from BioRad and an RI detector (Waters 2414).

The Faradaic Efficiency (FE) of gaseous product i (CO or H_2) is calculated in **Equation (1)**:

$$FE\,(i) == \frac{I_i}{I} = \frac{zF\varnothing_i v}{I} \quad (1)$$

Where z is the number of electrons transferred in the reaction (2 for CO and H_2), F is the Faraday constant (96485C mol^{-1}), $\varnothing_i$ is the volume fraction of the gaseous product in the sample, I is the instantaneous total current when GC sampling (A), and ν is the molar flow rate of the CO_2 gas (mol s^{-1}).

FE of formate production is calculated in **Equation** (2):

$$FE\,(formate) = \frac{zFc_{formate}V}{it} \tag{2}$$

Where $c_{formate}$ is the concentration of formate (mol L^{-1}), V is the total volume of catholyte (L), i is the total current of electrolysis (A), and t is the time of electrolysis (s).

Electrochemical impedance spectroscopy was collected from 1000 Hz to 1 Hz at 10 mV amplitude before electrolysis. The potentiostat compensated 85 % of the iR losses and the applied potentials were converted to the reversible hydrogen electrode (RHE) scale according to **Equation** (3) shown below:

$$E(RHE) = E(Ag/AgCl) + 0.2 + 0.0591pH \tag{3}$$

The double-layer capacitance (C_{dl}) was determined by recording CVs in a three-electrode cell consisting of a working electrode, an Ag/AgCl reference electrode, and an iridium wire as the counter electrode. The CVs were recorded between − 0.1 V and − 0.2 V (vs. Ag/AgCl) at different scan rates varying from 20 to 120 mV s^{-1} using CO_2-saturated 0.5 M $KHCO_3$.

2.5. In situ Raman

Titanium foil was used as the substrate for *in situ* Raman to avoid the interference of the strong carbon Raman signals, monitor the color change of the electrocatalysts, and improve the signal-to-noise ratio. For the electrode preparation, Mn-Bi_2O_3 or Bi_2O_3 catalyst powder was first collected by sonication of the Mn-Bi_2O_3 or Bi_2O_3 electrodes and further dried. 8 mg of the as-collected catalyst powder was dispersed in a mixture of 80 μL Nafion dispersion, and 320 μL 2-propanol, and then sonicated for 15 min. The above catalyst ink was spray-coated on a titanium foil to acquire a loading of 1.2 mg cm^{-2}. The as-prepared electrodes were assembled in a redox.me GDE Raman cell (see the cell configuration in **Scheme S3**). Raman spectra were recorded on Renishaw inVia^{TM} QONTOR Raman spectrometer instrument equipped with a 532 nm laser, a 2400 line mm^{-1} grating, 50x long working distance objective, and a CCD detector.

2.6. Computational details

All simulations were performed using spin-polarized Density functional theory (DFT) as implemented in the Vienna Ab initio Simulation Package [39,40]. The Generalized Gradient Approximation (GGA) PBE-D2 was the functional of choice [41–43]. Core electrons were described by PAW pseudopotentials [44,45], while valence electrons were expanded by plane wave basis sets with a kinetic energy cut-off of 450 eV. The Bi and Mn-doped Bi catalysts were modelled considering Bi (012), and BiMn(012) surfaces. Each contained four layers, where the two uppermost were fully relaxed and the rest were fixed to the bulk distances. Structures were relaxed with a force threshold smaller than 0.03 eV $Å^{-1}$. The Brillouin zone was sampled using a Γ-centered (3 × 2 × 1) k-points mesh for both surfaces, generated with the Monkhorst − Pack method [46]. The vacuum between the slabs was set to 12 Å in the z-direction.

For studied models, we obtained the Gibbs energies of relevant intermediates using $\Delta G = \Delta H + \Delta ZPE - T\Delta S$. To obtain the energies of the relevant intermediates in the electrochemical environment, the computational hydrogen electrode (CHE) was used [47,48]. The zero-point and entropic contributions are shown in **Tables S1-S2**. Further details on thermodynamic corrections are discussed in the **Supporting Information**.

3. Results and discussion

3.1. Synthesis and characterizations of electrodes

The binder-free catalyst materials were grown on the wet-proofed carbon paper (SEM images of the carbon paper are shown in **Figure S1**) by a facile solvothermal reaction followed by subsequent calcination in the air. As shown in Fig. 1**a** and **Figure S2**, Mn-Bi_2O_3 nanosheets are vertically and densely grown on the carbon fibers. In this way, the active material can form close contact with the conductive substrate, while the PTFE can still prevent possible flooding [32,33]. These nanosheets further overlap with each other to form a porous structure, which can facilitate mass transfer and provide a large surface area. Bi_2O_3 displays a similar structure, as shown by SEM in **Figure S3a-c**. The secondary structure of Mn-Bi_2O_3 and Bi_2O_3 were further examined by TEM. Undoped Bi_2O_3 shows nanosheet morphology with a 0.319 nm lattice distance corresponding to the (201) lattice spacing of β-Bi_2O_3 [49,50], and an even Bi/O elemental distribution (**Figure S3d-g**). However, images in Fig. 1**b-c** reveal that a few Mn-Bi_2O_3 nanosheets assemble into a nanoflower morphology. Each nanosheet further consists of ultrasmall nanoparticles with a lattice spacing slightly longer than 0.319 nm. Moreover, as can be seen in Fig. 1**d**, Bi and Mn are uniformly distributed over these nanoflowers.

The crystalline structures of the as-prepared undoped Bi_2O_3 and doped Mn-Bi_2O_3 are both β-Bi_2O_3 (PDF#27–0050) [38,51], as confirmed by XRD (Fig. 1**e**). Additional signals of impurities are not detected after Mn doping. The peak at around 18° on all electrodes is attributed to the (100) plane of PTFE (**Figure S1d**). We also observe that particularly the (201) XRD peak shifts to a lower angle (from 27.95 to 27.72°) after Mn-doping, further confirming the increase in the lattice spacing compared with undoped Bi_2O_3 (Fig. 1**e** and **Figure S4a**). The surface chemical composition of the electrodes (Fig. 1**f-g** and **Figure S5**) was characterized by using XPS. The Bi 4f doublet structure can be interpreted to have all Bi in the same 3 + chemical state corresponding to Bi_2O_3. The Mn-Bi_2O_3 exhibits the Mn 2p doublet at 641.77 eV and 653.27 eV shown in Fig. 1**g**. Based on the peak areas of Mn 2p and Bi 4f the Mn/Bi ratio on the surface is 3/100, which is close to the Mn content measured by ICP-OES (3.2 ± 0.4 % in **Table S3**), further demonstrating successful, homogeneous Mn doping. The F 1 s signal on both electrodes originates from the PTFE cover on the carbon paper (**Figure S5c** and **f**). To sum up, the Mn-Bi_2O_3 binder-free electrode is successfully prepared with the PTFE-modified carbon paper as a substrate.

3.2. Electrocatalytic performance

CO_2RR was investigated using the as-prepared working electrodes at room temperature in a customized flow cell with CO_2-saturated 0.5 M $KHCO_3$ electrolyte. Different ratios of Mn and Bi salts were used in the synthesis (see characterizations including XRD and SEM of these materials in **Figure S4**) and the amount of Mn was found to affect both the selectivity and reaction rate of CO_2RR (**Figure S6a-b**). The highest performance is achieved when 53 μmol of Mn salt together with 1 mmol of Bi salt was used. Therefore, this ratio was fixed for the synthesis and this sample is named as Mn-Bi_2O_3 (discussion on the characterizations in Section 3.1). The optimized Mn-Bi_2O_3 was then compared to the undoped Bi_2O_3. Cyclic voltammetry was first used to define a preferable potential range for CO_2RR. Mn-Bi_2O_3 shows a more positive onset potential at around − 0.64 V (vs. RHE), when compared to the one at around − 0.7 V (vs. RHE) for Bi_2O_3, and a higher current density (**Figure S6c**). Controlled-potential electrolysis at several applied potentials was further conducted based on the pre-defined potential range by CVs.

As demonstrated in Fig. 2**a-b**, H_2, and trace amounts of CO are the only gaseous products, while formate is the only liquid product generated during the controlled-potential electrolysis from − 0.7 V to − 1.2 V (vs. RHE). FE of formate on Mn-Bi_2O_3 gradually increases from − 0.7 V

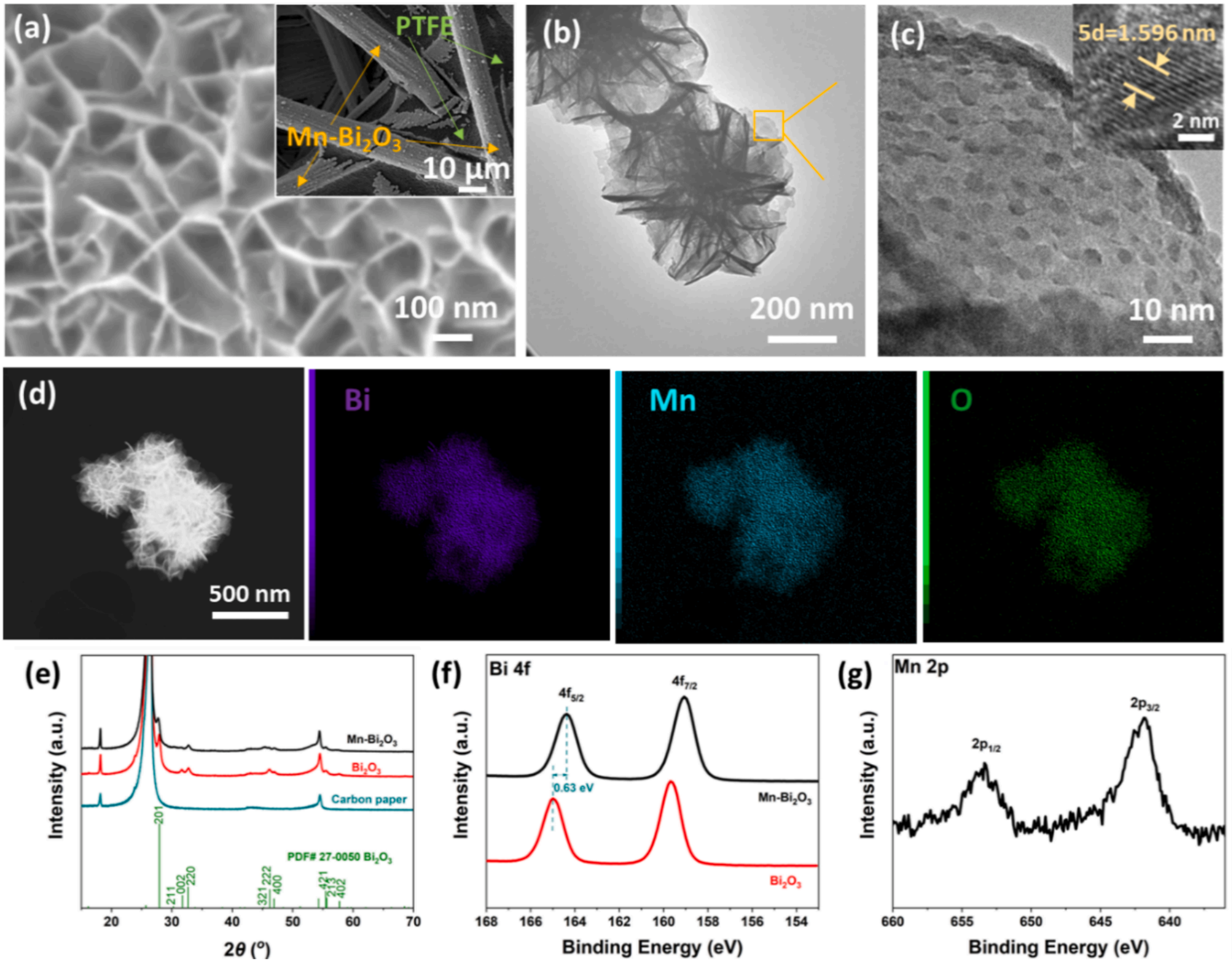

Fig. 1. (a) SEM images of Mn-Bi_2O_3. (b-c) TEM images of Mn-Bi_2O_3. (d) TEM-EDS mapping of Mn-Bi_2O_3. (e) XRD patterns of the electrodes. (f) Bi 4f high-resolution XPS spectra of Bi_2O_3 and Mn-Bi_2O_3. (g) Mn 2p high-resolution XPS spectrum of Mn-Bi_2O_3.

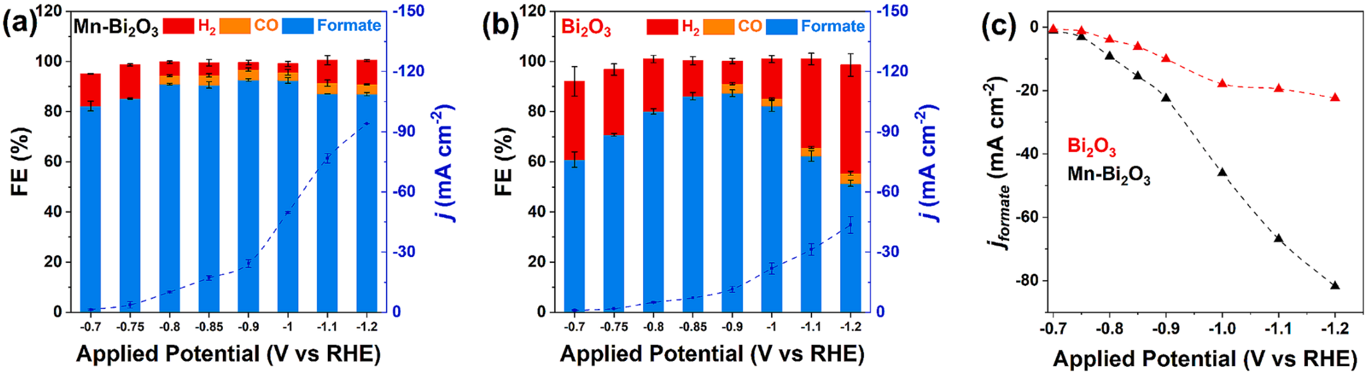

Fig. 2. Potential dependence of selectivity and total *j* over (a) Mn-Bi_2O_3 and (b) Bi_2O_3. (c) Partial *j* of formate over Mn-Bi_2O_3 and Bi_2O_3. All the measurements were conducted in CO_2-saturated 0.5 M $KHCO_3$ at room temperature.

to − 0.9 V (vs. RHE) followed by a slight decrease when more negative potentials are applied. On this electrode, the formate FE first achieves over 90.0 % at − 0.8 V (vs. RHE) and reaches a maximum of 92.6 % at − 0.9 V (vs. RHE). Even at − 1.2 V (vs. RHE), a high value of 87.0 % is observed. On the other hand, the undoped Bi_2O_3 electrode shows less than 80 % formate FE at − 0.8 V (vs. RHE) and reaches its maximum formate selectivity also at − 0.9 V (vs. RHE) with a value of only 87.0 %, which is more than 5 % lower compared to the Mn-Bi_2O_3 electrode. Shifting to more negative potentials from this optimum, a fast decline of formate FE is observed with only 51.4 % formate FE at − 1.2 V (vs. RHE). At the same time, the Mn-Bi_2O_3 electrode shows much higher total current densities in comparison to un-doped Bi_2O_3 (Fig. 2**a-b** and

Figure S7), which is in line with the findings of the CV measurements.

The formate partial current density on both electrodes increases with more negative applied potentials, with Mn-Bi_2O_3 showing more than twice higher currents than Bi_2O_3 at most potentials (Fig. 2**c**). Notably, Mn-Bi_2O_3 reaches around − 23 mA cm^{-2} of formate partial current density at − 0.9 V (vs. RHE), which is more than 300 mV lower overpotential than the one required for Bi_2O_3 to reach a comparable current density value. At − 1.2 V (vs. RHE), Mn-Bi_2O_3 shows over − 80 mA cm^{-2} formate partial current density, which is nearly 3 times higher than the one of Bi_2O_3. As shown above, an optimized amount of Mn doping enhances the catalytic performance of Bi_2O_3.

3.3. *Monitoring the active phase during CO_2RR*

As the key materials doped and undoped Bi_2O_3 have been reported to change phases during electrolysis [27,28], a few characterization techniques including *in situ* Raman, *ex situ* XRD, SEM, and TEM were applied to trace their evolution and to identify the active sites.

The materials were first monitored over time under exposure to the electrolyte at open circuit potential (OCP). Several Raman peaks at 125, 142, 315, and 464 cm^{-1} appear on a dry Bi_2O_3 electrode (Fig. 3**a**). These can be attributed to the displacements of cationic − Bi(III) − entities in the oxide surrounding (125 cm^{-1}) and Bi − O stretching mode in Bi_2O_3 (315 and 468 cm^{-1}), respectively [52,53]. These peaks become less dominant over time and finally nearly disappear after 20 min of exposure to the CO_2-saturated aqueous 0.5 M $KHCO_3$ electrolyte (Fig. 3**b**). At the same time, a new strong Raman peak appears and becomes dominant at 162 cm^{-1}, which can be assigned to $Bi_2(CO_3)O_2$ [27]. The electrode also undergoes a color change from bright yellow to pale white during this process (**Figure S9a-b**). The dry Mn-Bi_2O_3 electrode (Fig. 3**a** and **Figure S8a**) shows Raman peaks at 124, 313 and 475 cm^{-1}, also attributed to Bi_2O_3 [52,53], and a $Bi_2(CO_3)O_2$-related peak at 162 cm^{-1}, which may be due to the reaction with atmospheric CO_2 [27]. After exposure to the electrolyte, these peaks disappear nearly immediately (only the peak at 475 cm^{-1} can be observed at 0 min), and peaks related to $Bi_2(CO_3)O_2$ become dominant and stable after 4 min of electrolyte exposure (Fig. 3**c**). Several spots on dry Mn-Bi_2O_3 electrodes also show slightly different Raman spectra as their peaks at 313 cm^{-1} become broad while the peak at 475 cm^{-1} becomes sharper (**Figure S8a**). However, all measured spots show similar fast phase conversion from Bi_2O_3 to $Bi_2(CO_3)O_2$ upon exposure to the electrolyte (see **Figure S8b** for another example). Meanwhile, the color of the electrode changes from dark brown to light brown (**Figure S9e-f**). The Mn doping appears to accelerate the phase change from Bi_2O_3 to $Bi_2(CO_3)O_2$ and this phase change is in line with the *ex situ* XRD patterns of the electrodes used in the flow cell (**Figure S8c**).

Then, the phase transition under applied potentials was evaluated. As shown in **Figure S10a-b**, the intensity of the characteristic peak at 162 cm^{-1} in undoped $Bi_2(CO_3)O_2$ gradually decreases after 16 min at − 0.7 V (vs. RHE) in CO_2-saturated 0.5 M $KHCO_3$. On the contrary, this peak of Mn-doped $Bi_2(CO_3)O_2$ remains nearly unchanged even after 20 min. XRD patterns in **Figure S10c** confirm that after 20 min both electrodes used in the flow cell exhibit a mixture of metallic Bi and $Bi_2(CO_3)O_2$, while the intensity of metallic Bi is higher in the undoped electrode.

As the potential becomes more negative, the $Bi_2(CO_3)O_2$ peaks at − 0.9 V (vs. RHE) for both electrodes at 162 cm^{-1} nearly completely disappear during the study as shown in Fig. 4**a-b**. However, a new broad signal appears at around 184 cm^{-1}, which could be attributed to the reoxidation of metallic Bi by laser stimulation [54]. The rate of the phase change for the undoped material is faster, as presented in Fig. 3**d-e** (within 2 min for the undoped electrode and approximately 14 min for the Mn-doped electrode, respectively). The color of the undoped electrode turns almost completely black (**Figure S9c-d**) while the surface of the Mn-doped electrode becomes darker brownish (**Figure S9f-g**).

XRD patterns of the electrodes used in the flow cell (Fig. 4**c**) confirm that after 20 min of electrolysis, nearly all undoped $Bi_2(CO_3)O_2$ has converted to metallic Bi. However, after the same time of electrolysis, the Mn-doped electrode still maintains mainly $Bi_2(CO_3)O_2$ with only low-intensity metallic Bi peaks (Fig. 4**d**). With a longer testing time, the $Bi_2(CO_3)O_2$ gradually disappears with the intensity of the metallic Bi peak strengthened also on Mn-doped material.

SEM analysis of the Mn-doped electrode after different electrolysis durations in the flow cell is shown in Fig. 4**e**. Mn-doped $Bi_2(CO_3)O_2$ retains the original nanosheet morphology within the initial 10 min of CO_2RR. As the electrolysis time increases, the previous flat nanosheets gradually shrink into nanoparticles with irregular edges. Finally, nearly all the nanosheets become nanoparticles after 60 min, and this morphological change is similar to a previous study [55]. The undoped electrodes show a faster morphological change as nanoparticles dominate after only 20 min as shown in **Figure S11**. The characterization results show that although Mn doping slows down the reduction from $Bi_2(CO_3)O_2$ to metallic Bi, the phase will become metallic Bi eventually.

The secondary structure of the active materials from the Mn-doped electrode were further characterized with TEM. After over 30-min saturation in the electrolyte, the nanosheet becomes porous with a lattice distance of 0.31 nm corresponding to the (013) lattice spacing of $Bi_2(CO_3)O_2$ (**Figure S12**). Bi, O, C, and Mn are found to be uniformly distributed over both nanostructures according to the EDS mapping. TEM images of active materials after 60-min electrolysis at − 0.9 V (vs. RHE) are shown in Fig. 4**f-g**, and the observed nanoparticles in above-mentioned SEM are made of smaller nanoparticles aggregation with a lattice distance of 0.328 nm corresponding to the (012) lattice spacing of metallic Bi. Due to the oxyphilic nature of Bi, those small nanoparticles are covered with an amorphous oxide layer. Bi and Mn remain uniformly distributed over both nanostructures according to the EDS mapping shown in Fig. 4**h**.

Due to the quick reduction of the undoped electrode (proved by both *in situ* Raman and *ex situ* XRD), we propose that the metallic Bi is the

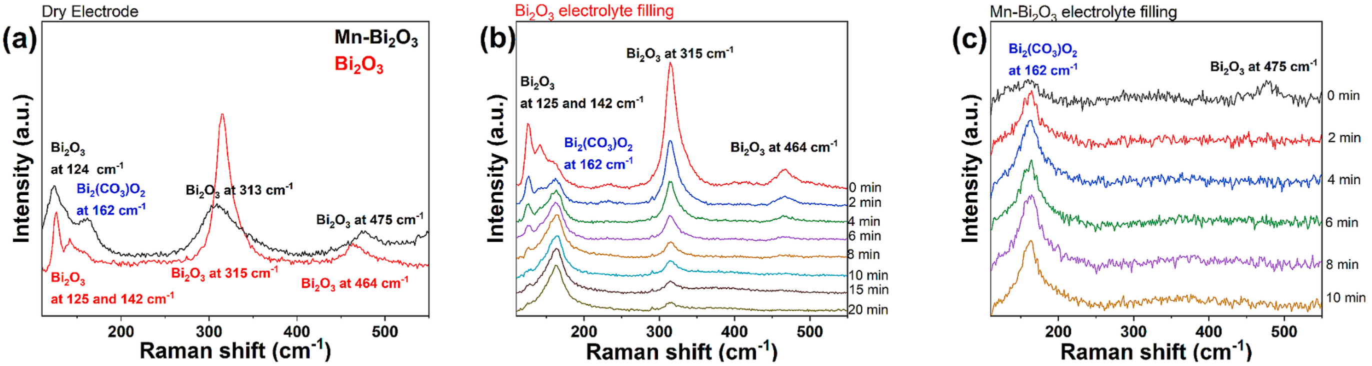

Fig. 3. (a) Raman spectra of dry electrodes. Time-dependent *in situ* Raman spectra of (b) Bi_2O_3 and (c) Mn-Bi_2O_3 with CO_2-saturated 0.5 M $KHCO_3$ at room temperature.

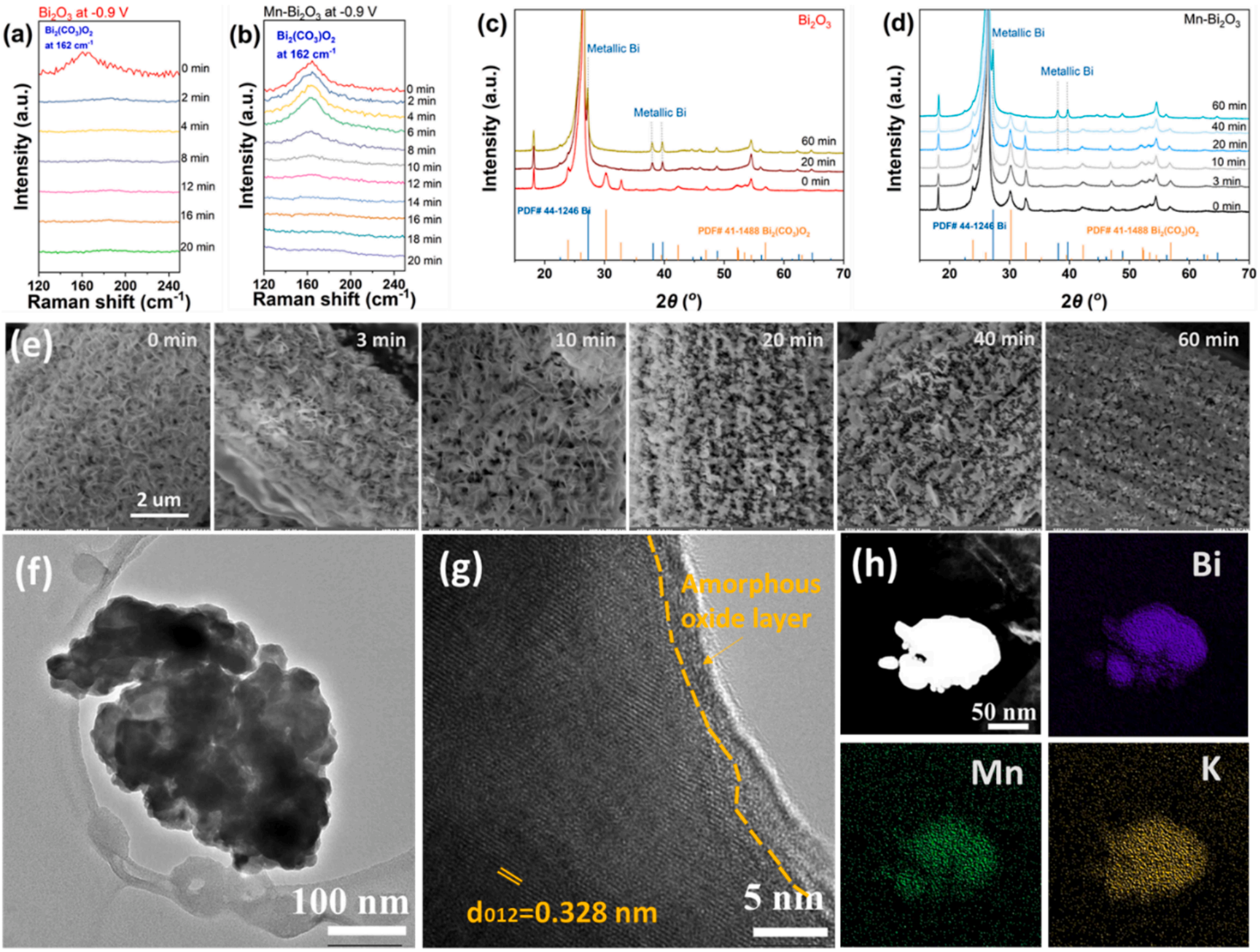

Fig. 4. Phase and morphological changes under a cathodic potential. The electrodes have been saturated in CO_2-saturated 0.5 M $KHCO_3$ at room temperature for over 30 min before starting the experiments. All experiments were conducted using CO_2-saturated 0.5 M $KHCO_3$ at room temperature. Time-dependent *in situ* Raman spectra of (a) Bi_2O_3 and (b) Mn-Bi_2O_3 at − 0.9 V (vs. RHE). XRD patterns of (c) the Bi_2O_3 and (d) Mn-Bi_2O_3 electrodes at different electrolysis time at − 0.9 V (vs. RHE) in the flow cell. (e) SEM images of the Mn-Bi_2O_3 electrodes after different electrolysis time at − 0.9 V (vs. RHE) in CO_2-saturated 0.5 M $KHCO_3$ in the flow cell. The scale is the same for all the images. (f-g) TEM images of Mn-Bi_2O_3 after 60 min of electrolysis at − 0.9 V (vs. RHE). (h) Dark-field TEM image and EDS mapping images of Mn-Bi_2O_3 after 60 min of electrolysis at − 0.9 V (vs. RHE).

active site for CO_2RR. For the Mn-doped electrode, the situation may vary. At − 0.7 V (vs. RHE) the catalytic sites may be both Mn-doped $Bi_2(CO_3)O_2$ and (Mn-modified) metallic Bi, while at − 0.9 V (vs. RHE), Mn-modified metallic Bi is plausibly the active site. However, longer electrolysis time and postmortem characterization should be carried out to confirm that (further analysis in **section 3.5**).

3.4. Reaction mechanism analysis

To assess the enhancement of CO_2RR through Mn-doping, the electrochemical active surface area (ECSA) was initially measured by evaluating the C_{dl}. The Mn-Bi_2O_3 sample exhibits a C_{dl} that is approximately 27 % higher than that of Bi_2O_3 (2.25 vs. 1.77 mF cm^{-2}, respectively), indicating a greater number of exposed active sites (**Figure S13a-c**). Even when normalized against ECSA, the formate current density of Mn-Bi_2O_3 remains higher than that of undoped Bi_2O_3 (**Figure S13d**). This further demonstrates the superior intrinsic catalytic activity of Mn-Bi_2O_3 for CO_2RR.

DFT calculations were then performed to examine the impact of Mn doping on the electronic structure of the Bi(012) surface and its subsequent effect on formate formation. To understand the influence of Mn on the charge distribution of the surrounding Bi atoms, a Bader charge analysis and partial density of states (pDOS) evaluation of the Bi(012) and BiMn(012) surfaces were performed (Fig. 5). The Bader analysis (Fig. 5**a**) shows that the Bi atoms surrounding Mn are more negatively charged compared to those on the Bi(012) surface, as Mn acts as an electron donor, which is in line with the negative shift of the Bi peaks in the XPS spectra (Fig. 1**f**). Furthermore, Fig. 5**b** displays the calculated p-orbital pDOS of the Bi atom adjacent to Mn in the BiMn(012) surface and the Bi atom in the same position in the Bi(012) surface. When comparing both surfaces, the pDOS of BiMn(012) reveals a slightly higher electronic density at the Fermi level. This increase is due to the transfer of electrons from Mn into the p orbital of Bi, causing the p orbital of Bi on the BiMn(012) surface to become delocalized, which can activate CO_2. However, as Mn donates electrons, it becomes favorable for CO_2 activation because the hybridization between the d-orbital of Mn and the *π orbital of CO_2 is weaker.

Then, the $CO_2^{\bullet-}$ intermediate adsorption energy on $MnBi_4$ (BiMn (012)) is first compared with that on the MnN_4C model [56] at − 0.6 V (vs. RHE). The adsorption energy on the $MnBi_4$ model is 0.90 eV, which is 0.35 eV higher than the 0.45 eV observed for the MnN_4 system, where the MnN_4 catalyst is known to produce CO. However, when Bi surrounds

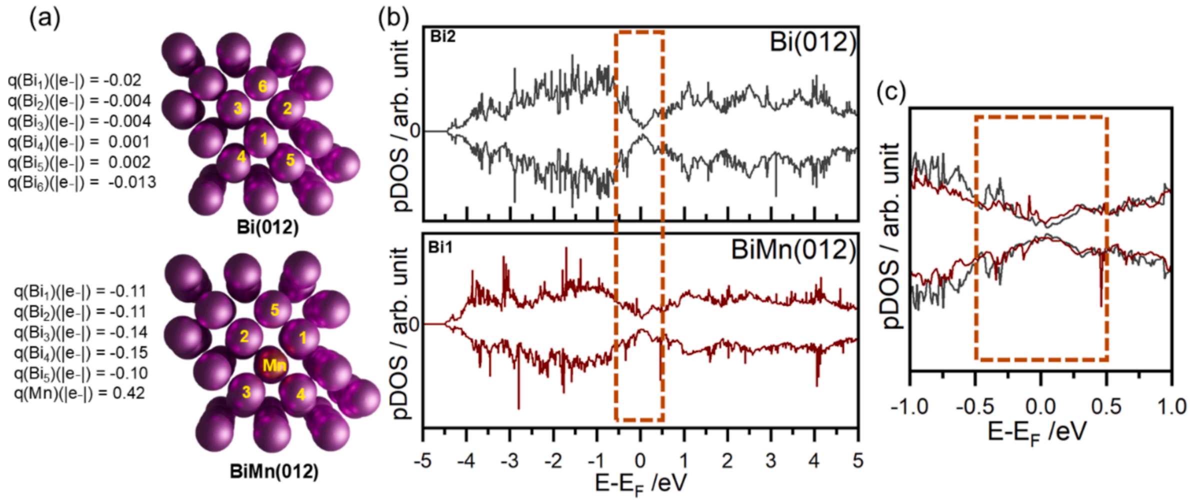

Fig. 5. (a) Bader analysis of the Bi(112) and BiMn(112) surfaces. (b) The projected density of states (pDOS) for the 6p orbital of two distinct Bi atoms in the Bi(012) and BiMn(012) surfaces is evaluated, with the Fermi level set to zero. (c) Zoomed pDOS plot of both Bi(Bi) and BiMn(012) surfaces.

Mn, the charge becomes less positive, resulting in CO_2 adsorbing with lower energy, which could lead to formate formation. According to the rule, catalysts that weakly bind the $CO_2^{\bullet -}$ intermediate tend to facilitate proton attacks on the carbon of the free radical, resulting in the formation of $HCOO^-/HCOOH$. Conversely, a strongly bonded $CO_2^{\bullet -}$ intermediate leads to the formation of CO, as the proton attacks an oxygen atom [57]. Therefore, Mn doping appears to alter the electronic properties of Bi(012), allowing the *OCHO intermediate to adsorb and desorb more easily. As we could not obtain the $CO_2^{\bullet -}$ intermediate on the Bi(012) surface, the mechanism is analyzed via two coupled electron and proton transfers:

(i) $CO_{2(g)} + H^+ + e^- \rightarrow *OCHO$
(ii) $*OCHO + H^+ + e^- \rightarrow *OCHOH$
(iii) $*OCHOH \rightarrow HCOOH_{(aq)} + *$,

which produces *OCHO and *OCHOH intermediates and the final release of $HCOO^-/HCOOH$. The tested sites are illustrated in Fig. 6**a**. The adsorption energy of *OCHO on the central atom (site 1), the Bi and Mn atoms, and the Bi atom above the central atom (site 2) are compared for both surfaces. The Gibbs free energy diagram (Fig. 6**b**) shows that the intermediates (*OCHO, *OCHOH) adsorbed on site 1 of the BiMn(012) surface have higher free energy than those on Bi(012), indicating that BiMn(012) more easily desorbs $HCOO^-/HCOOH$. When *OCHO is adsorbed on site 2 on BiMn(012), the adsorption becomes unfavorable, whereas for Bi(012), the free energy of *OCHO is 0.28 eV lower than on site 1. The structures of the adsorbed intermediates are shown in **Figure S14**. Additionally, we investigated the reaction mechanism involving the *COOH intermediate on site 1. As shown in **Figure S15**, the energy barrier for the reaction via *COOH is significantly higher, making it unlikely to occur.

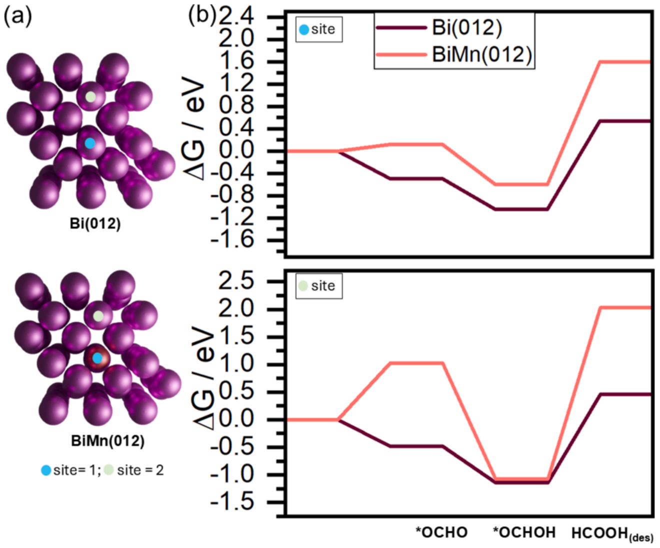

Fig. 6. (a) Tested sites for HCOOH formation, and (b) Gibbs free energy profiles of reaction mechanism toward $HCOO^-/HCOOH$ formation over Bi(012) and BiMn(012) at − 0.9 V (vs. RHE).

These findings suggest that Mn itself has become an active site. Moreover, the reduced charge transfer resistance of the Mn-doped electrode (**Figure S13e**), compared to the undoped electrode, can enhance both steps i and ii.

3.5. *Comparison of stability using different substrates*

Stability is another important factor in the evaluation of an electrode and material. The PTFE-modified wet-proofed carbon paper was specifically chosen as the substrate to diminish flooding. As shown in Fig. 7**a**, a continuous 60-hour electrolysis on Mn-Bi_2O_3 was carried out at − 25 mA cm^{-2}. The potential remains nearly unchanged at around − 0.9 V (vs. RHE), and the formate FE just decreases slightly from 92.7 % to 88.1 % indicating good stability of the performance.

Postmortem SEM and TEM images in **Figure S16** show the nanoparticle morphology, which is similar to that after 60 min electrolysis (Fig. 4**a**). The XRD pattern (**Figure S17a**) shows mainly metallic Bi with only a few $Bi_2(CO_3)O_2$ remaining. The high-resolution XPS Bi spectrum in **Figure S17b** depicts that the chemical composition is Bi^{3+}, which may result from unreacted $Bi_2(CO_3)O_2$ residue on the surface or the re-oxidation of metallic Bi before the XPS measurement. Mn still maintains a uniform distribution in these metallic Bi nanoparticles as shown in TEM-EDS (**Figure S16e**) with Mn signal also detectable on the surface as shown in the high-resolution XPS Mn 2p spectrum (**Figure S17c**). The bulk Mn content is quite similar before and after the stability test as shown in the ICP-OES results (**Table S3**). As the catalytic activity remains quite similar after 1 h, and the phase and morphology also stay unchanged after testing for 60 h, it is confirmed that Mn-modified Bi should be the active site. Moreover, the similar PTFE-covered surface in the SEM images (**Figure S16**), the XRD peak at around 18° (**Figure S17a**), and the F 1 s signal in XPS (**Figure S17d**), all demonstrate that there is no chemical composition change of the PTFE during long-term electrolysis.

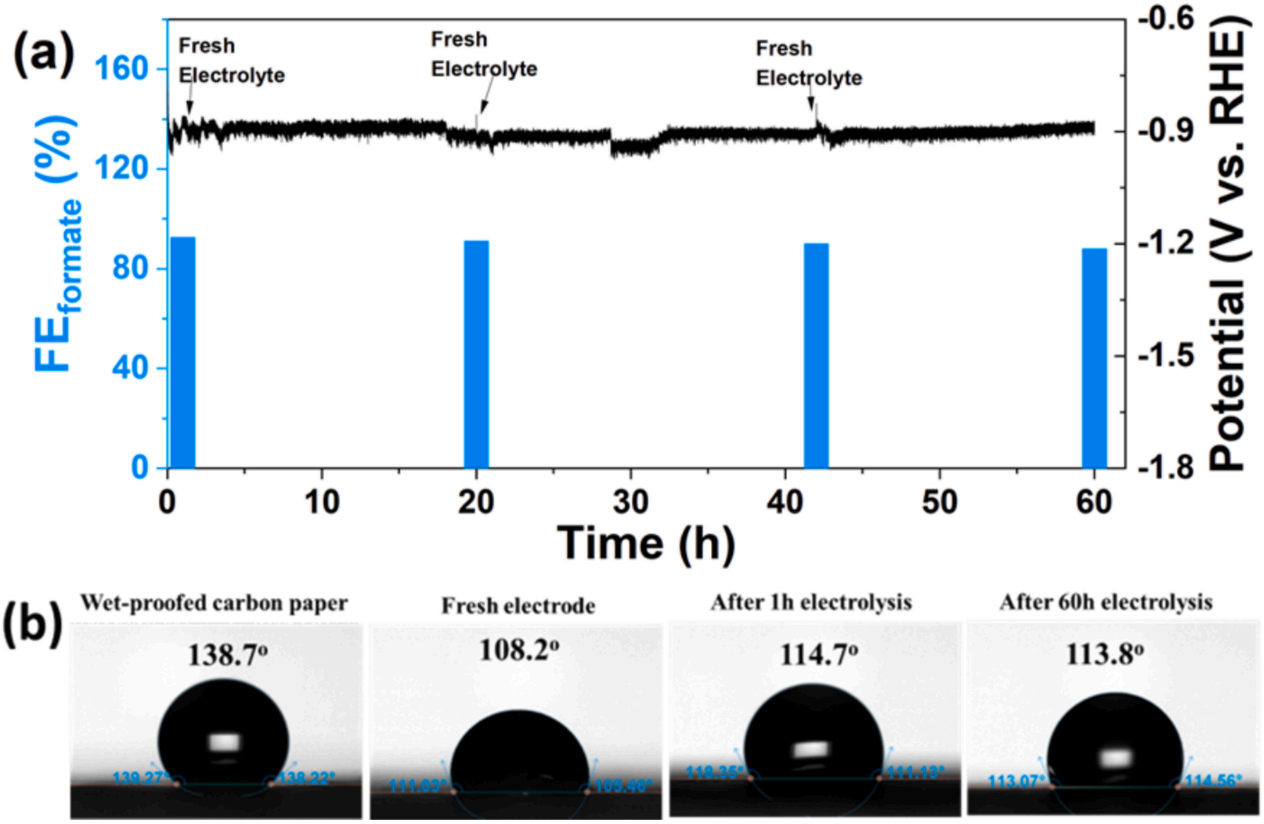

Fig. 7. (a) Long-term stability measurements at − 25 mA cm^{-2} on Mn-Bi_2O_3 in CO_2-saturated 0.5 M $KHCO_3$ at room temperature. (b) Contact angle measurements of substrates and electrodes at different stages.

To further elucidate the importance of PTFE modification in long-term stability, two additional substrates (unmodified and hydrophilic carbon paper) were tested. Carbon fibers in unmodified and hydrophilic carbon paper are quite similar to those in wet-proofed carbon paper, but there are PTFE aggregates in wet-proofed carbon paper as shown in Figure S1**a-c**. Interestingly, if the carbon paper was not pre-treated with PTFE before the Mn-Bi_2O_3 synthesis, the formate FE of this Mn-Bi_2O_3 on unmodified carbon paper is quite similar when compared to the studied Mn-Bi_2O_3 during the initial first hour of electrolysis (93.0 %). However, after 20 h and 40 h of electrolysis the formate FE drops to 80.5 % and finally to 73.2 % on the unmodified carbon paper-supported material, respectively (Figure S18**a**). If this unmodified carbon paper was further treated into very hydrophilic before the Mn-Bi_2O_3 synthesis, the material shows only 81.2 % formate FE during the first hour and significant decay to 58.5 % after 20 h of electrolysis (Figure S18**b**). In addition, the potential continues to increase during the 20 h test, indicating the electrode is not suitable for long-term use.

Flooding is mainly suspected to cause stability issues. Therefore, contact angle measurements were carried out on all the electrodes at different stages of electrolysis as shown in Fig. 7**b** and Figure S18**c-d**. Wet-proofed and unmodified carbon paper both show a highly hydrophobic feature while after acid treatment the unmodified carbon paper becomes hydrophilic as expected. After growing Mn-Bi_2O_3 on the electrodes, both the unmodified and hydrophilic carbon paper electrodes become hydrophilic. However, owing to PTFE on Mn-Bi_2O_3, the electrode based on the wet-proofed carbon paper still maintains a hydrophobic feature. This electrode is still hydrophobic even after 60 h of electrolysis. In contrast, the electrolyte droplet is almost instantly absorbed by the surface on unmodified carbon paper after 40 h electrolysis as it turns out to be extremely hydrophilic. For Mn-Bi_2O_3 grown on the hydrophilic carbon paper, the same change occurs already within 20 h. The complete wetting of the above-mentioned two electrodes will cause flooding due to the lack of hydrophobic domains in the electrode. This may block the gaseous CO_2 transport pathways to the active sites. The electrolyte saturation will further promote salt precipitation, leading to the eventual permeant blockage of the CO_2 transport pathways and reduced active area. This further verifies the stability-improving effects of wet-proofed substrates, which is consistent with previous studies [32,33,58].

4. Conclusion

In conclusion, we fabricated a binder-free Mn-doped Bi_2O_3 electrode for CO_2RR. It exhibits enhanced performance at all potentials when compared with undoped Bi_2O_3. *In situ* Raman, XRD, SEM, and TEM were used to study the changes in the active materials Mn-Bi_2O_3 and Bi_2O_3 under reaction conditions. Both the doped and undoped Bi_2O_3 transform into $Bi_2(CO_3)O_2$ with the $KHCO_3$ electrolyte, and Mn-doping accelerates this phase change. Under applied potential, both Mn-doped and undoped $Bi_2(CO_3)O_2$ undergo a reduction to metallic Bi. Although Mn-doping slows down $Bi_2(CO_3)O_2$ reduction to metallic Bi, the whole electrode eventually converts to Mn-modified Bi within 1 h of electrolysis. Therefore, metallic Bi and Mn-modified Bi are suggested to be the real sites under potentials for CO_2RR. The DFT analysis demonstrates that doping Bi(012) with Mn effectively enhances selectivity through *OCHO intermediate. Charge transfer occurs from Mn to the surrounding Bi atoms, where the interaction makes Mn less negatively charged, resulting in a weaker binding to CO_2 and facilitating formate production. Furthermore, the use of wet-proofed carbon paper as the substrate extends the stability of Mn-Bi_2O_3 to over 60 h by mitigating flooding compared to using non-PTFE modified or hydrophilic substrate. This study offers in-depth insights into the design and understanding of doped BiO_x-based electrodes for CO_2 reduction.

CRediT authorship contribution statement

Junjie Shi: Writing – original draft, Visualization, Methodology, Investigation, Formal analysis, Conceptualization. **Paulina Pršlja:** Writing – original draft, Visualization, Methodology, Investigation, Formal analysis. **Milla Suominen:** Writing – review & editing, Supervision, Methodology, Investigation. **Benjin Jin:** Writing – review & editing, Investigation. **Jouko Lahtinen:** Writing – review & editing, Investigation, Formal analysis. **Lilian Moumaneix:** Writing – review & editing, Investigation. **Xiangze Kong:** Writing – review & editing, Investigation. **Tanja Kallio:** Writing – review & editing, Validation, Supervision, Resources, Project administration, Funding acquisition, Data curation, Conceptualization.

Declaration of competing interest

The authors declare that they have no known competing financial interests or personal relationships that could have appeared to influence the work reported in this paper.

Acknowledgments

The provision of facilities and technical support by Aalto University at OtaNano Nanomicroscopy Center (Aalto-NMC) and RAMI infrastructures are acknowledged. We thank Ms. Constanza Gallegos Herrera for assistance in operating ICP-OES. Computational resources for this project were obtained from CSC-IT Center for Science and Aalto University's Science-IT project. J. S., M. S. and T. K. thank Jane and Aatos Erkko Foundation (the USVA project) and the Research Council of Finland (the Profi 7 project, 142210501) for financial support. P. P. gratefully acknowledges funding from the Research Council of Finland under the C1 Value Programme, project No. 329483.

Appendix A. Supplementary material

Supplementary data to this article can be found online at https://doi.org/10.1016/j.jcat.2024.115798.

Data availability

Data will be made available on request.

References

[1] D.U. Nielsen, X.M. Hu, K. Daasbjerg, T. Skrydstrup, Chemically and electrochemically catalysed conversion of CO_2 to CO with follow-up utilization to value-added chemicals, Nat. Catal. 1 (2018) 244–254, https://doi.org/10.1038/s41929-018-0051-3.

[2] R. Kortlever, J. Shen, K.J.P. Schouten, F. Calle-Vallejo, M.T.M. Koper, Catalysts and reaction pathways for the electrochemical reduction of carbon dioxide, J. Phys. Chem. Lett. 6 (2015) 4073–4082, https://doi.org/10.1021/acs.jpclett.5b01559.

[3] N. Han, P. Ding, L. He, Y. Li, Y. Li, Promises of main group metal-based nanostructured materials for electrochemical CO_2 reduction to formate, Adv. Energy Mater. 10 (2020) 1902338, https://doi.org/10.1002/aenm.201902338.

[4] Y. Guan, M. Liu, X. Rao, Y. Liu, J. Zhang, Electrochemical reduction of carbon dioxide (CO_2): Bismuth-based electrocatalysts, J. Mater. Chem. A 9 (2021) 13770–13803, https://doi.org/10.1039/d1ta01516h.

[5] D. Xia, H. Yu, H. Xie, P. Huang, R. Menzel, M.M. Titirici, G. Chai, Recent progress of Bi-based electrocatalysts for electrocatalytic CO_2 reduction, Nanoscale 14 (2022) 7957–7973, https://doi.org/10.1039/d2nr01900k.

[6] S. Yang, M. Jiang, W. Zhang, Y. Hu, J. Liang, Y. Wang, Z. Tie, Z. Jin, In situ structure refactoring of bismuth nanoflowers for highly selective electrochemical reduction of CO_2 to formate, Adv. Funct. Mater. 33 (2023) 202301984, https://doi.org/10.1002/adfm.202301984.

[7] M. Wu, Y. Xiong, B. Hu, Z. Zhang, B. Wei, L. Li, J. Hao, W. Shi, Indium doped bismuth subcarbonate nanosheets for efficient electrochemical reduction of carbon dioxide to formate in a wide potential window, J. Colloid Interface Sci. 624 (2022) 261–269, https://doi.org/10.1016/j.jcis.2022.05.054.

[8] M. Zhang, W. Wei, S. Zhou, D.D. Ma, A. Cao, X.T. Wu, Q.L. Zhu, Engineering a conductive network of atomically thin bismuthene with rich defects enables CO_2 reduction to formate with industry-compatible current densities and stability, Energy Environ. Sci. 14 (2021) 4998–5008, https://doi.org/10.1039/d1ee01495a.

[9] Q. Gong, P. Ding, M. Xu, X. Zhu, M. Wang, J. Deng, Q. Ma, N. Han, Y. Zhu, J. Lu, Z. Feng, Y. Li, W. Zhou, Y. Li, Structural defects on converted bismuth oxide nanotubes enable highly active electrocatalysis of carbon dioxide reduction, Nat. Commun. 10 (2019) 2807, https://doi.org/10.1038/s41467-019-10819-4.

[10] X. An, S. Li, X. Hao, X. Du, T. Yu, Z. Wang, X. Hao, A. Abudula, G. Guan, Thein situmorphology transformation of bismuth-based catalysts for the effective electroreduction of carbon dioxide, Sustain. Energy Fuels 4 (2020) 2831–2840, https://doi.org/10.1039/d0se00228c.

[11] T. Gao, X. Wen, T. Xie, N. Han, K. Sun, L. Han, H. Wang, Y. Zhang, Y. Kuang, X. Sun, Morphology effects of bismuth catalysts on electroreduction of carbon dioxide into formate, Electrochim. Acta 305 (2019) 388–393, https://doi.org/10.1016/j.electacta.2019.03.066.

[12] S. Liu, X.F. Lu, J. Xiao, X. Wang, X.W. (David) Lou, Bi_2O_3 Nanosheets Grown on Multi-Channel Carbon Matrix to Catalyze Efficient CO_2 Electroreduction to HCOOH, Angew. Chem. Int. Ed. 58 (2019) 13828–13833. Doi: 10.1002/anie.201907674.

[13] R. Yu, C. Qiu, Z. Lin, H. Liu, J. Gao, S. Li, Y. Yao, J. Yu, S. Yang, CeO_x promoted electrocatalytic CO_2 reduction to formate by assisting in the critical hydrogenation step, ACS Mater. Lett. 4 (2022) 1749–1755, https://doi.org/10.1021/acsmaterialslett.2c00512.

[14] C. Wang, R. Pang, Z. Pan, Y. Zhu, C. Li, B. Liu, J. Shen, The interfacial aspect of Bi_2O_3/CeO_x heterostructure catalysts for HCOOH production from CO_2 electroreduction, J. Mater. Chem. A 10 (2022) 22694–22700, https://doi.org/10.1039/d2ta06640h.

[15] Y. Zhao, X. Liu, Z. Liu, X. Lin, J. Lan, Y. Zhang, Y.R. Lu, M. Peng, T.S. Chan, Y. Tan, Spontaneously Sn-doped Bi/BiO_xCore-shell nanowires toward high-performance CO_2 electroreduction to liquid fuel, Nano Lett. 21 (2021) 6907–6913, https://doi.org/10.1021/acs.nanolett.1c02053.

[16] G. Zhang, X. Zheng, X. Cui, J. Wang, J. Liu, J. Chen, Q. Xu, Doping of vanadium into bismuth oxide nanoparticles for electrocatalytic CO_2 reduction, ACS Appl. Nano Mater. 5 (2022) 15465–15472, https://doi.org/10.1021/acsanm.2c03503.

[17] F. Tian, T. Tang, X. Di, X. Guo, D. Liu, Y. Shi, Z. Shen, X. Yu, X. Shao, Single-atom iron doped BiOCl atomic layers to promote efficient CO_2 electroreduction towards formate, Catal. Sci. Technol. 14 (2023) 62–65, https://doi.org/10.1039/d3cy01523h.

[18] H. Wei, A. Tan, Z. Xiang, J. Zhang, J. Piao, Z. Liang, K. Wan, Z. Fu, Modulating p-orbital of bismuth nanosheet by nickel doping for electrocatalytic carbon dioxide reduction reaction, ChemSusChem 15 (2022) e202200752, https://doi.org/10.1002/cssc.202200752.

[19] H. Shen, Y. Zhao, L. Zhang, Y. He, S. Yang, T. Wang, Y. Cao, Y. Guo, Q. Zhang, H. Zhang, In-situ constructuring of copper-doped bismuth catalyst for highly efficient CO_2 electrolysis to formate in ampere-level, Adv. Energy Mater. 13 (2023) 202202818, https://doi.org/10.1002/aenm.202202818.

[20] Y. Liu, T. Wu, H. Cheng, J. Wu, X. Guo, H.J. Fan, Active plane modulation of Bi_2O_3 nanosheets via Zn substitution for efficient electrocatalytic CO_2 reduction to formic acid, Nano Res. 16 (2023) 10803–10809, https://doi.org/10.1007/s12274-023-5824-6.

[21] P.A. Hsieh, P.J. Chen, L.M. Lyu, S.Y. Chen, M.C. Tseng, M.Y. Chung, W.H. Chiang, J.L. Chen, C.H. Kuo, Enhanced production of formic acid in electrochemical CO_2 reduction over Pd-doped BiOCl nanosheets, ACS Appl. Mater. Interfaces 13 (2021) 58799–58808, https://doi.org/10.1021/acsami.1c20009.

[22] X. Peng, Y. Chen, Y. Mi, L. Zhuo, G. Qi, J. Ren, Y. Qiu, X. Liu, J. Luo, Efficient electroreduction CO_2 to CO over MnO_2 nanosheets, Inorg. Chem. 58 (2019) 8910–8914, https://doi.org/10.1021/acs.inorgchem.9b01018.

[23] H. Han, S. Jin, S. Park, Y. Kim, D. Jang, M.H. Seo, W.B. Kim, Plasma-induced oxygen vacancies in amorphous MnO_x boost catalytic performance for electrochemical CO_2 reduction, Nano Energy 79 (2021) 105492, https://doi.org/10.1016/j.nanoen.2020.105492.

[24] Y. Chae, K. Kim, H. Yun, D. Kim, W. Jung, Y.J. Hwang, U. Lee, D.K. Lee, B.K. Min, W. Choi, D.H. Won, Tailoring electrochemical CO_2 reduction via substrate-induced gas diffusion, J. Mater. Chem. A 11 (2023) 7025–7033, https://doi.org/10.1039/d3ta00617d.

[25] T. Wissink, A.J.W. Man, W. Chen, J.M.J.J. Heinrichs, R.C.J. van de Poll, M. C. Figueiredo, E.J.M. Hensen, Evolution of bismuth oxide catalysts during electrochemical CO_2 reduction, J. CO2 Util. 77 (2023) 102604, https://doi.org/10.1016/j.jcou.2023.102604.

[26] J. Ma, J. Yan, J. Xu, J. Ni, H. Zhang, L. Lu, Dynamic ion exchange engineering BiOI-derived $Bi_2O_2CO_3$ to promote CO_2 electroreduction for efficient formate production, Chem. Eng. J. 455 (2023) 140926, https://doi.org/10.1016/j.cej.2022.140926.

[27] A. Dutta, I. Zelocualtecatl Montiel, K. Kiran, A. Rieder, V. Grozovski, L. Gut, P. Broekmann, A Tandem ($Bi_2O_3 \rightarrow Bi_{met}$) catalyst for highly efficient *ec*-CO_2 conversion into formate: *Operando* Raman spectroscopic evidence for a reaction pathway change, ACS Catal. 11 (2021) 4988–5003, https://doi.org/10.1021/acscatal.0c05317.

[28] Y. Yuan, Q. Wang, Y. Qiao, X. Chen, Z. Yang, W. Lai, T. Chen, G. Zhang, H. Duan, M. Liu, H. Huang, In situ structural reconstruction to generate the active sites for CO_2 electroreduction on bismuth ultrathin nanosheets, Adv. Energy Mater. 12 (2022) 202200970, https://doi.org/10.1002/aenm.202200970.

[29] Y. Gong, T. He, Gaining deep understanding of electrochemical CO_2RR with in situ/operando techniques, Small Methods 7 (2023) 202300702, https://doi.org/10.1002/smtd.202300702.

[30] J. Chen, B. Ma, Z. Xie, W. Li, Y. Yang, M. Mu, X. Zou, B. Zhao, W. Song, Bifunctional porous SnO_2/Ag nanofibers for efficient electroreduction of carbon dioxide to formate and its mechanism elucidation by in-situ surface-enhanced

Raman scattering, Appl. Catal. B Environ. 325 (2023) 122350, https://doi.org/10.1016/j.apcatb.2022.122350.

[31] F. Pan, Y. Yang, Designing CO_2 reduction electrode materials by morphology and interface engineering, Energy Environ. Sci. 13 (2020) 2275–2309, https://doi.org/10.1039/d0ee00900h.

[32] L. Li, J. Chen, V.S.S. Mosali, Y. Liang, A.M. Bond, Q. Gu, J. Zhang, Hydrophobicity graded gas diffusion layer for stable electrochemical reduction of CO_2, Angew. Chem. Int. Ed. 61 (2022) e202208534, https://doi.org/10.1002/anie.202208534.

[33] K. Yang, R. Kas, W.A. Smith, T. Burdyny, Role of the carbon-based gas diffusion layer on flooding in a gas diffusion electrode cell for electrochemical CO_2 reduction, ACS Energy Lett. 6 (2021) 33–40, https://doi.org/10.1021/acsenergylett.0c02184.

[34] M.E. Leonard, L.E. Clarke, A. Forner-Cuenca, S.M. Brown, F.R. Brushett, Investigating electrode flooding in a flowing electrolyte, gas-fed carbon dioxide electrolyzer, ChemSusChem 13 (2020) 400–411, https://doi.org/10.1002/cssc.201902547.

[35] Y. Wu, L. Charlesworth, I. Maglaya, M.N. Idros, M. Li, T. Burdyny, G. Wang, T. E. Rufford, Mitigating electrolyte flooding for electrochemical CO_2 reduction via infiltration of hydrophobic particles in a gas diffusion layer, ACS Energy Lett. 7 (2022) 2884–2892, https://doi.org/10.1021/acsenergylett.2c01555.

[36] D. Wu, G. Huo, W.Y. Chen, X.Z. Fu, J.L. Luo, Boosting formate production at high current density from CO_2 electroreduction on defect-rich hierarchical mesoporous Bi/Bi_2O_3 junction nanosheets, Appl. Catal. B Environ. 271 (2020) 118957, https://doi.org/10.1016/j.apcatb.2020.118957.

[37] M. Chen, J. Bi, X. Huang, T. Wang, Z. Wang, H. Hao, Bi_2O_3 nanosheets arrays in-situ decorated on carbon cloth for efficient electrochemical reduction of nitrate, Chemosphere 278 (2021) 130386, https://doi.org/10.1016/j.chemosphere.2021.130386.

[38] L. Zhang, Y. Shi, Z. Wang, C. Hu, B. Shi, X. Cao, Porous β-Bi_2O_3 with multiple vacancy associates on highly exposed active 220 facets for enhanced photocatalytic activity, Appl. Catal. B Environ. 265 (2020) 118563, https://doi.org/10.1016/j.apcatb.2019.118563.

[39] G. Kresse, J. Furthmüller, Efficiency of ab-initio total energy calculations for metals and semiconductors using a plane-wave basis set, Comput. Mater. Sci. 6 (1996) 15–50, https://doi.org/10.1016/0927-0256(96)00008-0.

[40] G. Kresse, J. Furthmüller, Efficient iterative schemes for ab initio total-energy calculations using a plane-wave basis set, Phys. Rev. B 54 (1996) 11169–11186, https://doi.org/10.1103/PhysRevB.54.11169.

[41] A. Allouche, Software news and updates gabedit — A graphical user interface for computational chemistry softwares, J. Comput. Chem. 32 (2012) 174–182, https://doi.org/10.1002/jcc.21600.

[42] J.P. Perdew, K. Burke, M. Ernzerhof, Generalized gradient approximation made simple, Phys. Rev. Lett. 77 (1996) 3865–3868, https://doi.org/10.1103/PhysRevLett.77.3865.

[43] T. Bučko, J. Hafner, S. Lebègue, J.G. Ángyán, Improved description of the structure of molecular and layered crystals: Ab initio DFT calculations with van der Waals corrections, J. Phys. Chem. A 114 (2010) 11814–11824, https://doi.org/10.1021/jp106469x.

[44] P.E. Blöchl, Projector augmented-wave method, Phys. Rev. B 50 (1994) 17953–17979, https://doi.org/10.1103/PhysRevB.50.17953.

[45] G. Kresse, D. Joubert, From ultrasoft pseudopotentials to the projector augmented-wave method, Phys. Rev. B 59 (1999) 1758–1775, https://doi.org/10.1103/PhysRevB.59.1758.

[46] H.J. Monkhorst, J.D. Pack, Special points for Brillonln-zone integrations, Phys. Rev. B 13 (1976) 5188–5192, https://doi.org/10.1103/PhysRevB.13.5188.

[47] A.A. Peterson, F. Abild-Pedersen, F. Studt, J. Rossmeisl, J.K. Nørskov, How copper catalyzes the electroreduction of carbon dioxide into hydrocarbon fuels, Energy Environ. Sci. 3 (2010) 1311–1315, https://doi.org/10.1039/c0ee00071j.

[48] J.K. Nørskov, J. Rossmeisl, A. Logadottir, L. Lindqvist, J.R. Kitchin, T. Bligaard, H. Jónsson, Origin of the overpotential for oxygen reduction at a fuel-cell cathode, J. Phys. Chem. B 108 (2004) 17886–17892, https://doi.org/10.1021/jp047349j.

[49] C. Yu, P. Yang, L. Tie, S. Yang, S. Dong, J. Sun, J. Sun, One-pot fabrication of β-Bi_2O_3@Bi_2S_3 hierarchical hollow spheres with advanced sunlight photocatalytic RhB oxidation and Cr(VI) reduction activities, Appl. Surf. Sci. 455 (2018) 8–17, https://doi.org/10.1016/j.apsusc.2018.04.201.

[50] Y. Shi, L. Luo, Y. Zhang, Y. Chen, S. Wang, L. Li, Y. Long, F. Jiang, Synthesis and characterization of α/β-Bi_2O_3 with enhanced photocatalytic activity for 17α-ethynylestradiol, Ceram. Int. 43 (2017) 7627–7635, https://doi.org/10.1016/j.ceramint.2017.03.057.

[51] J. In, I. Yoon, K. Seo, J. Park, J. Choo, Y. Lee, B. Kim, Polymorph-tuned synthesis of α- and β-Bi_2O_3 nanowires and determination of their growth direction from polarized raman single nanowire microscopy, Chem. Eur. J. 17 (2011) 1304–1309, https://doi.org/10.1002/chem.201001684.

[52] B. Ávila-Bolívar, M. Lopez Luna, F. Yang, A. Yoon, V. Montiel, J. Solla-Gullón, S. W. Chee, B. Roldan Cuenya, Revealing the intrinsic restructuring of Bi_2O_3 nanoparticles into Bi nanosheets during electrochemical CO_2 reduction, ACS Appl. Mater. Interfaces 16 (2024) 11552–11560, https://doi.org/10.1021/acsami.3c18285.

[53] C. Díaz-Guerra, P. Almodóvar, M. Camacho-López, S. Camacho-López, J. Piqueras, Formation of β-Bi_2O_3 and δ-Bi_2O_3 during laser irradiation of Bi films studied in-situ by spatially resolved Raman spectroscopy, J. Alloy Compd. 723 (2017) 520–526, https://doi.org/10.1016/j.jallcom.2017.06.263.

[54] L. Kumari, J.H. Lin, Y.R. Ma, Laser oxidation and wide-band photoluminescence of thermal evaporated bismuth thin films, J. Phys. D Appl. Phys. 41 (2008) 025405, https://doi.org/10.1088/0022-3727/41/2/025405.

[55] X. Wei, W. Zhang, D. Liu, D. Liu, Y. Yan, J. Zhang, Y. Yang, S. Yan, Z. Zou, Bi particles with exposed (012) facet on 3D substrate as highly active and durable electrode for CO_2 reduction to formate, J. CO2 Util. 55 (2022) 101797, https://doi.org/10.1016/j.jcou.2021.101797.

[56] J. Li, P. Pršlja, T. Shinagawa, A.J. Martín Fernández, F. Krumeich, K. Artyushkova, P. Atanassov, A. Zitolo, Y. Zhou, R. García-Muelas, N. López, J. Pérez-Ramírez, F. Jaouen, Volcano trend in electrocatalytic CO_2 reduction activity over atomically dispersed metal sites on nitrogen-doped carbon, ACS Catal. 9 (2019) 10426–10439, https://doi.org/10.1021/acscatal.9b02594.

[57] F. Lü, H. Bao, Y. Mi, Y. Liu, J. Sun, X. Peng, Y. Qiu, L. Zhuo, X. Liu, J. Luo, Electrochemical CO_2 reduction: From nanoclusters to single atom catalysts, Sustain. Energy Fuels 4 (2020) 1012–1028, https://doi.org/10.1039/c9se00776h.

[58] J. Shi, N. Han, B. Jin, M. Suominen, J. Lahtinen, K. Miikki, B.P. Wilson, T. Kallio, Construction of hydrophilic-hydrophobic domains in Bi_2O_3/nitrogen-doped carbon electrode to boost CO_2-to-formate conversion, Next Mater. 3 (2024) 100183, https://doi.org/10.1016/j.nxmate.2024.100183.